Microsc. Microanal. Page 1 of 10
doi:10.1017/S1431927613014001

Microscopy AND Microanalysis

EBSD Analysis of Tungsten-Filament Carburization During the Hot-Wire CVD of Multi-Walled Carbon Nanotubes

Clive J. Oliphant,[1,2,*] Christopher J. Arendse,[1] Sigqibo T. Camagu,[3] and Hendrik Swart[4]

[1]*Department of Physics, University of the Western Cape, Private Bag X17, Bellville 7535, South Africa*
[2]*National Metrology Institute of South Africa, Private Bag X34, Lynwood Ridge, Pretoria 0040, South Africa*
[3]*Council for Scientific and Industrial Research, Light Metals, Pretoria 0001, South Africa*
[4]*Department of Physics, University of the Free State, Bloemfontein, 9300, South Africa*

Abstract: Filament condition during hot-wire chemical vapor deposition conditions of multi-walled carbon nanotubes is a major concern for a stable deposition process. We report on the novel application of electron backscatter diffraction to characterize the carburization of tungsten filaments. During the synthesis, the W-filaments transform to W_2C and WC. W-carbide growth followed a parabolic behavior corresponding to the diffusion of C as the rate-determining step. The grain size of W, W_2C, and WC increases with longer exposure time and increasing filament temperature. The grain size of the recrystallizing W-core and W_2C phase grows from the perimeter inwardly and this phenomenon is enhanced at filament temperatures in excess of 1,400°C. Cracks appear at filament temperatures >1,600°C, accompanied by a reduction in the filament operational lifetime. The increase of the W_2C and recrystallized W-core grain size from the perimeter inwardly is ascribed to a thermal gradient within the filament, which in turn influences the hardness measurements and crack formation.

Key words: chemical vapor deposition, tungsten filament, carburization, microhardness, electron backscatter diffraction

Introduction

Versatility of the hot-wire chemical vapor deposition (HWCVD) technique is reflected in its application to synthesize a diverse range of materials such as hydrogenated silicon thin films (Mahan et al., 1991), diamond films (Moustakas, 1989), carbon microcoils (Chen et al., 2008; Oliphant et al., 2009*a*), polymer films (Pryce Lewis et al., 2009), and carbon nanotubes (CNTs) (Dillon et al., 2003). During the HWCVD process, the precursors are dissociated by a resistively heated filament resulting in reactive species that can react with each other *en route* to a substrate where eventual material deposition occurs. However, the dissociated species can react with the heated filament causing it to undergo structural transformations, a process referred to as filament aging. Consequently, the thermal, electrical, and mechanical properties of the filament changes, which can lead to an unstable deposition process.

Various protocols such as heating the filament in vacuum and a molecular hydrogen (H_2) ambient (Knoesen et al., 2008; van der Werf et al., 2009) and using low deposition pressures (<0.5 kPa) (Tabata & Niato, 2011) were implemented to slow down the filament aging process and increase its operational lifetime for synthesizing C- and Si-based materials. Recently, Kawale et al. (2011) employed HWCVD to synthesize CNTs using natural plant-derived precursors such as camphor instead of conventional hydrocarbons like methane (CH_4) and acetylene. Nevertheless, the use of CH_4 at high deposition pressures is promising for large-scale synthesis of multi-walled carbon nanotubes (MWCNTs) using HWCVD (Dillon et al., 2003).

Despite the efforts to reduce filament aging, the filament alloying process is still being investigated. Previous studies have focused primarily on linking microscopy, X-ray diffraction (XRD), elemental energy-dispersive X-ray spectroscopy (EDS), Auger electron spectroscopy (AES), X-ray photoelectron spectroscopy (XPS), and *in situ* resistance to characterize the filament carburizing process at low deposition pressures (Kromka et al., 2001; Zeiler et al., 2002; Oliphant et al., 2009*b*; Shi et al., 2011; Tabata & Niato, 2011).

In this contribution, we present the application of electron backscatter diffraction (EBSD) analysis to investigate the W-filament carburization process during the HWCVD of high-quality MWCNTs at high-deposition pressures and CH_4 flow rates (Arendse et al., 2007). Specifically, the effect of the microstructural properties of the carburized filament, such as grain sizes and orientation, on its mechanical properties/stability was investigated.

Materials and Methods

A quartz tube-based HWCVD system designed for the deposition of CNTs was used to carburize W-filaments (Arendse et al., 2007). Commercially pure W-filaments (diameter 500 μm and length 35 cm) were coiled and exposed to a CH_4:H_2 ambient at a pressure of 20 kPa. The CH_4 and H_2 flow rates were fixed at 10 and 100 sccm, respectively. The filament temperature (T_{fil}) was varied from 1,400 to 2,000°C, as measured by a two-color optical pyrometer. At

Received August 23, 2013; accepted November 26, 2013
*Corresponding author. E-mail: coliphant@nmisa.org

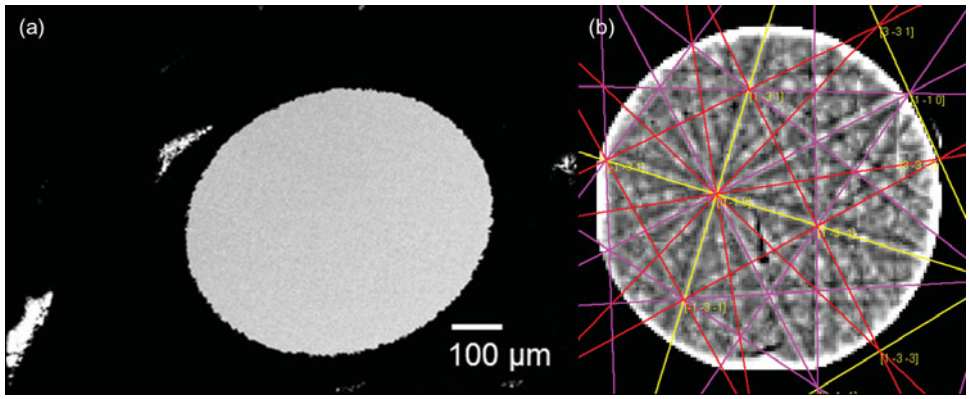

Figure 1. a: Cross-section backscatter electron image of as-received W-filament. **b:** Solved Kikuchi patterns of the W-filament shown in (**a**).

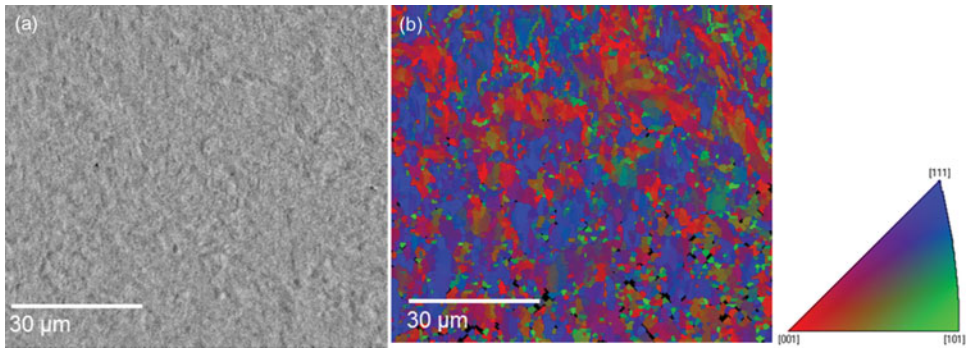

Figure 2. a: Backscatter electron and (**b**) corresponding electron backscatter diffraction grain orientation map (with key) of the as-received filament at higher magnification.

each filament temperature the deposition time was varied to 5, 15, 30, and 60 min. In other sets of experiments, pure W-filaments were heated to ∼2,000°C for 15 min in a N_2 and a H_2 ambient at a pressure of 20 kPa. In each case, the filaments were allowed to cool down in vacuum.

Portions of the filaments were then crushed, on which XRD measurements were performed using a PANalytical Xpert PRO diffractometer operated at 45 kV and 40 mA. XRD patterns were collected in reflection geometry at 2θ-values ranging from 10 to 90° with a step size of 0.02°. Copper K_α radiation with a wavelength of 1.5406 Å was used as the X-ray source. Parts from the central hottest region of the filament were mounted and mechanically prepared for metallography. Final polishing was performed using colloidal silica. Scanning electron microscopy (SEM), EDS, and, EBSD were performed in a LEO 1525 FEGSEM. Standardless EDS and EBSD analysis were performed in the Oxford INCA Energy and Crystal software, respectively. The acceleration voltage for EBSD and EDS analysis was set to 25 and 5 kV, respectively. The W and C chemical composition of the cross-section of the filament carburized at 1,800°C was also determined using AES performed in a PHI 700 Scanning Auger Nanoprobe at an acceleration voltage and emission current of 5 kV and 10 nA, respectively. The surface was sputtered for 1 min at an acceleration voltage of 2 kV and current of 2 μA before the AES surveys. XPS measurements were carried out on the cross-sections of the aged filament using a PHI 5000 Versaprobe Scanning ESCA Microprobe. The excitation source was a monochromatic Al X-ray beam at 15 kV and 12.5 W. SXI images were recorded with a 10 μm Al X-ray beam at 15 kV and 1.25 W. The samples were sputtered for 2 min with a 2 kV and 2 μA beam of Ar ions. Vickers microhardness measurements were carried out using an FM-700® Microhardness Tester. Indentations were performed at a load of 0.05 kg and a dwell time of 10 s.

Results

Figure 1 presents a backscatter electron (BSE) micrograph of the as-received W-filament. The filament diameter amounted to 550 μm within standard deviation (SD) 25 μm and is composed of W-grains with an average size of ∼1 μm as shown by the orientation map (OM) in Figure 2. During the deposition, however, the W-filament experiences significant structural changes. As seen in the BSE micrographs of the aging filament, shown in Figure 3, an ∼120 μm thick layer appears after 5 min of exposure to the CH_4:H_2 ambient. Cracks within this layer appear to extend from the perimeter radially inward. These cracks grow with increasing carburization time. The filament diameter remained constant for $T_{\text{fil}} \leq$ 1,600°C during the first 60 min of carburization. However, the diameter enhanced by ∼9% after 60 min at $T_{\text{fil}} \geq$ 1,800°C.

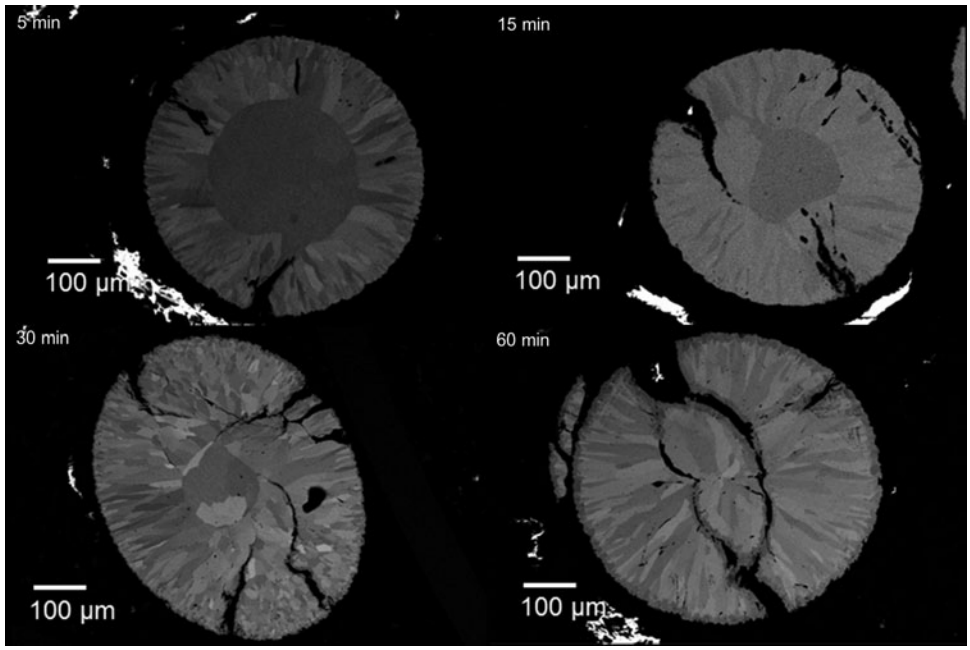

Figure 3. Cross-section backscatter electron micrographs of the filament carburized in a CH_4:H_2 ambient for different times at 1,800°C.

EDS analysis performed on random areas within the layer discloses that it is composed of 36.27 at% C and 63.73 at% W (SD 5 at%), roughly corresponding to the W_2C phase. The inner core is composed of ~10 at% C and 90 at% W. Also noticeable is that the layer appears to be "brighter" than the core, despite the higher C content of the former. Atomic number differences are therefore not the only cause behind the observed BSE image contrast within the W_2C layer in Figure 3. In the case of tantalum filament silicidation (Oliphant et al., 2012) it was found that the grain orientation with respect to the incident electron beam also contributes to the contrast in a BSE image.

Figure 4 shows EBSD phase maps of the filament carburized at T_{fil} = 2,000°C. The EBSD analysis validates the EDS findings that the layer is W_2C and the core is predominately W. Also present is the WC phase, which exists at the outer perimeter of the filament and regions where cracks were formed. The W_2C layer is approximately four times thicker at 5 min compared to the W-filament carburization process at HWCVD conditions of diamond (Zeiler et al., 2002). The W_2C phase is enhanced with prolonged exposure and eventually consumes the W at 60 min for T_{fil} = 1,800°C and at 30 min when T_{fil} = 2,000°C.

Figure 5 displays AES analysis performed on the different regions of contrast within the filament carburized at 1,800°C for 30 min. The O and N signals originate from exposing the filament to air before the AES measurements. The AES quantification reveals that the C content decreases moving radially inward within the filament, corresponding to the EDS analysis. The C content within the carbide layer varies between 24 and 46 at% relative to W, corresponding to the W_2C phase (Kurlov & Gusev, 2006), and confirming

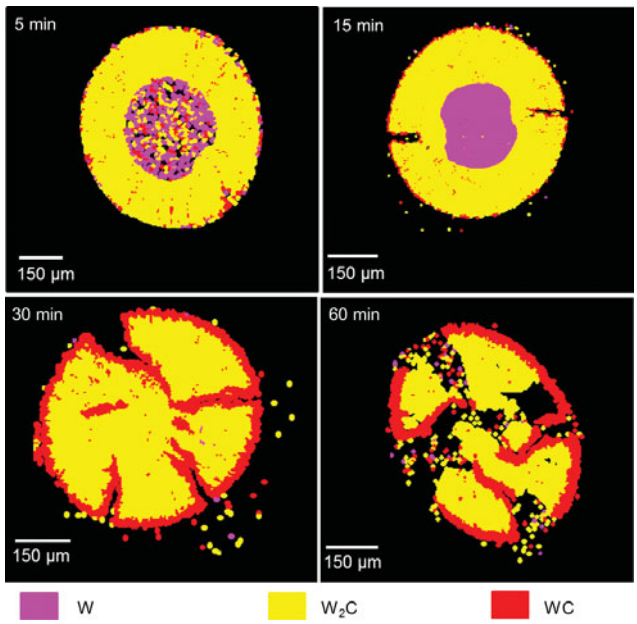

Figure 4. Electron backscatter diffraction phase maps of the carburizing W-filament cross-sections heated to 2,000°C for different durations.

the EBSD analysis. The inner core is a W-rich phase with a C content of ~10 at% C, similar to the findings of the EDS analysis. The outer layer contains a C content in excess of 60 at%, consistent with the WC phase (Kurlov & Gusev, 2006).

XPS further validated the EDS and AES analysis. Figure 6 displays the XPS wide scans of the W-filament carburized at 1,800°C for 30 min. The inner core consists of close to 100 at% W, consistent with the W phase. The layer at the

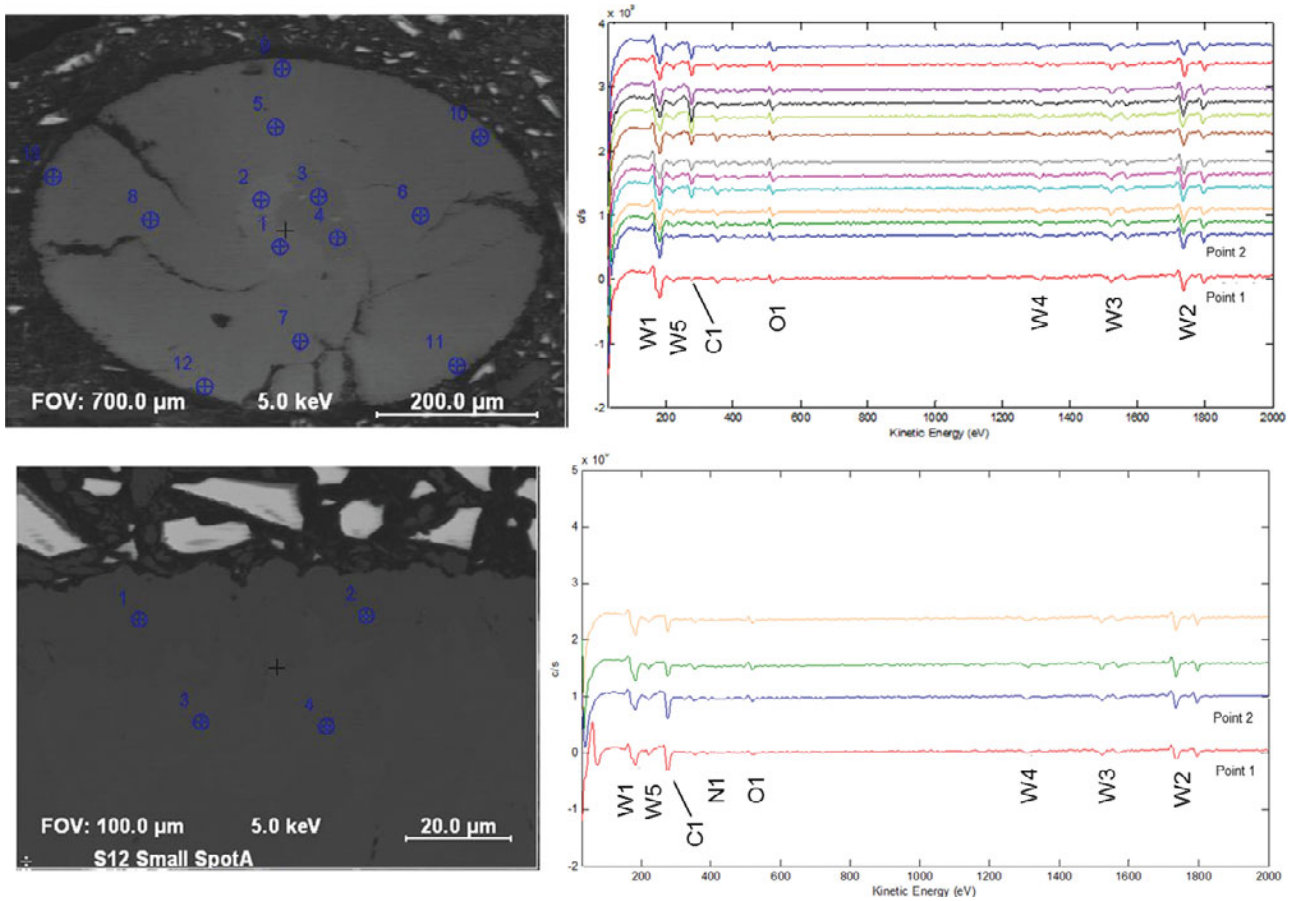

Figure 5. Scanning electron microscopy images showing locations of Auger electron spectroscopy point analysis and corresponding spectra of a W-filament carburized for (**a**) 30 and (**b**) 60 min.

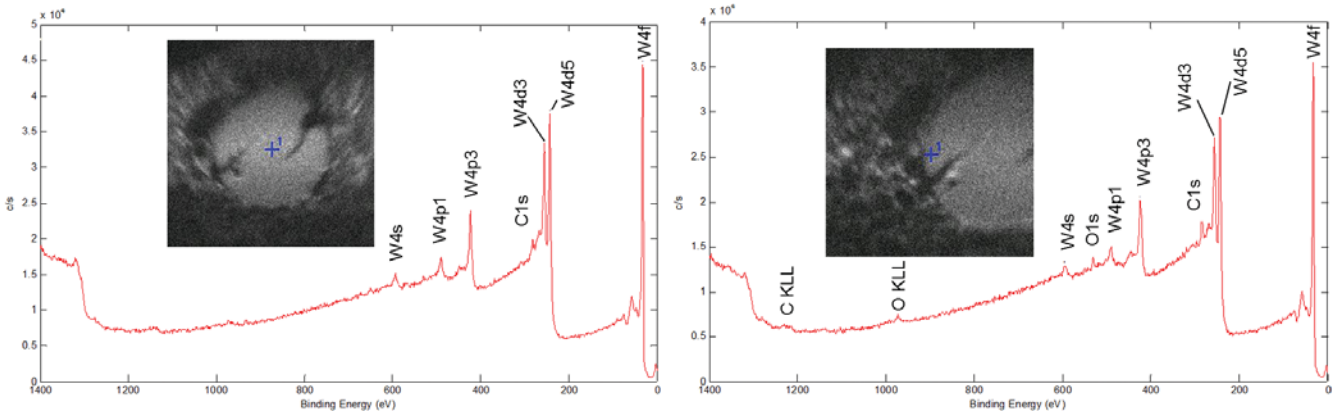

Figure 6. X-ray photoelectron spectroscopy spectra from different areas of the cross-section of the W-filament carburized for 30 min at 1,800°C.

outer perimeter of the filament is composed of ~56 at% C and 44 at% W, which corresponds to the WC phase. XPS point analysis within the bulk of the cross-section of the filament carburized for 60 min at 1,800°C, which mostly consists of W_2C according to EBSD, reveal that the C and W content amounted to 30 and 70 at%, respectively.

Figure 7 shows EBSD OM of the W_2C phase at 30 min at varying filament temperatures. Interestingly, the W_2C grain size enhances with time and radially inward as illustrated by the BSE images shown in Figure 8. This observation highlights typical nucleation and growth processes, i.e., the W_2C phase grows from the perimeter, subsequently extending radially inward.

Table 1 shows the average grain sizes of the W_2C phase as a function of temperature and time. The grain sizes were determined from the EBSD software using the equivalent circle diameter values and the line intercept method (LIM); BSE images were also used to gauge the LIM values from

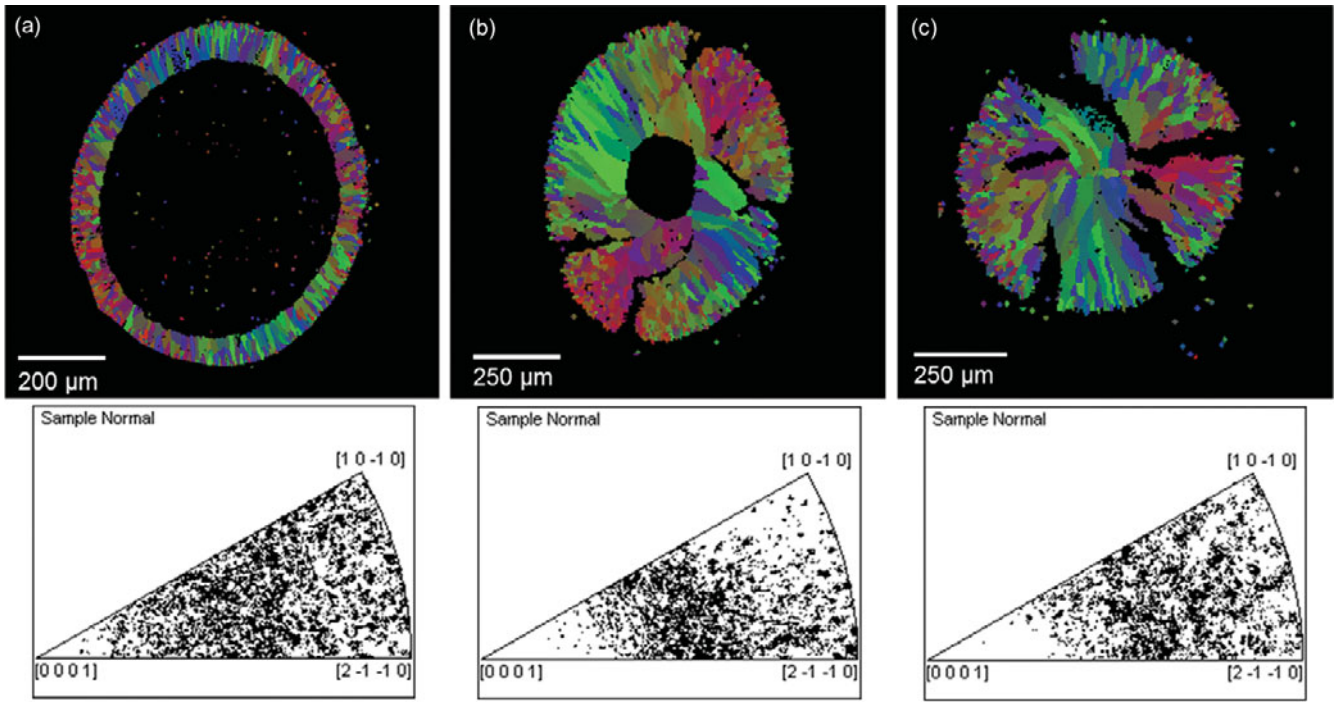

Figure 7. Grain orientation maps of the W_2C phase after 30 min at (**a**) 1,600°C, (**b**) 1,800°C, and (**c**) 2,000°C. The inverse pole figures below correspond to each orientation map above.

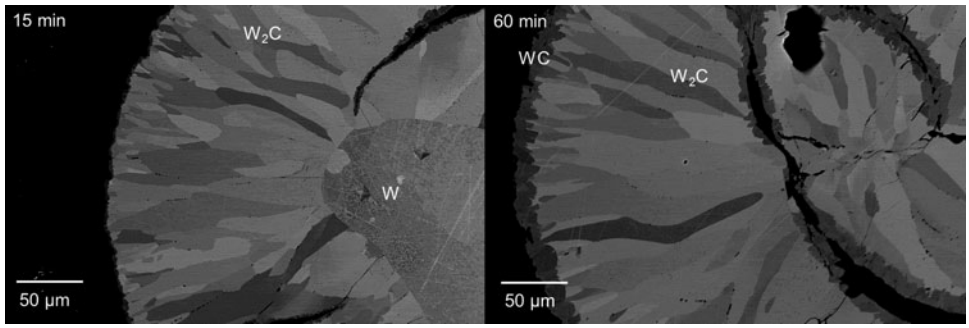

Figure 8. Backscatter electron micrographs of the filaments carburized at T_{fil} = 1,800°C revealing the effect of different exposure times on the W_2C grain size.

the SEM. The different methods used to determine the average W_2C grain size showed acceptable correlations, regardless of the irregular shaped grains and <50 grains counted in most cases.

The W_2C layer thickness was determined using dimensional measurements in the SEM and is presented in Figure 9. In contrast to the findings in the case of diamond deposition (Zeiler et al., 2002), the growth of the W_2C layer exhibits a parabolic rate constant, indicating that the diffusion of C through the carbide is the rate-determining step. Nevertheless, the W_2C layer formed so rapidly that kinetic measurements were only possible in a few cases.

Similar to the W_2C phase, the W-core experienced an increase in grain size during carburization. Figure 10 shows W OMs at different filament temperatures, disclosing that during carburization the W-grains recrystallized and formed preferential orientations along the filament length. The

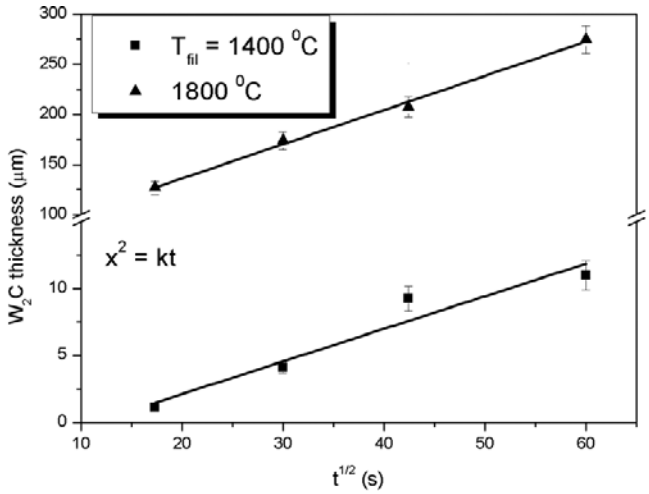

Figure 9. Growth kinetics of the W_2C layer at different filament temperatures.

Table 1. W_2C Grain Sizes Determined Using Different Approaches.*

T_{fil} (°C)	Time (min)	LIM_{SEM} (μm)	LIM_{EBSD} (μm)	ECD (μm)
1,600	30	9.0 ± 4.5	8.3 ± 1.0	12.9
	60	10.9 ± 8.3	5.6 ± 2.0	7.4
1,800	15	18.8 ± 13.8	18.0 ± 6.6	20.4
	30	24.4 ± 18.3	24.4 ± 10.6	28.0
	60	26.6 ± 16.9	24.1 ± 10.3	33.8
2,000	15	15.6 ± 6.2	14.2 ± 3.2	16.5
	30	23.4 ± 12.0	22.7 ± 9.0	27.1
	60	23.9 ± 17.2	23.4 ± 9.4	30.3

*The accuracy is determined largely by the irregular grain shapes and counting <50 grains in most cases. LIM, line intercept method; SEM, scanning electron microscopy; EBSD, electron backscatter diffraction; ECD, equivalent circle diameter.

W-recrystallization was further investigated in an H_2 and N_2 ambient. Figure 11 presents W OMs of as-received W-filaments heated to ~2,000°C for 15 min. Noticeable is the difference in the preferred orientation and the relatively smaller grain sizes in the H_2 ambient. Exposing the filaments to a H_2 and a CH_4:H_2 ambient results in a temperature drop of ~100°C, i.e. more power is needed to heat the filament to a temperature similar to that in a N_2 ambient or vacuum.

Vickers hardness measurements performed on at least three random areas in the recrystallized W-filaments reveal that the hardness depends on the grain size and orientation. Specifically, grains oriented in the [001] direction have a Vickers hardness of ~407 $HV_{0.05}$ (SD 10 HV). In contrast, grains oriented in the [111] and [100] directions display a hardness of ~450 (SD 23 HV) $HV_{0.05}$. Additionally, smaller grains at the perimeter in the H_2 case (Fig. 11b) have a superior hardness of ~496 $HV_{0.05}$. Nevertheless, the hardness of the W-filaments decreased substantially from 616 $HV_{0.05}$ (SD 14 HV) for the as-received filament as a result of the recrystallization. The influence of W crystal orientation on the microhardness has been observed before (Lassner & Schubert, 1999) and can be attributed to different number of W-atoms aligned along the indentation direction.

The hardness of the carbides were more scattered compared to the W-phase. The microhardness of the W_2C and WC phases amounted to 2,254 $HV_{0.05}$ (SD 140 HV) and 1,777 $HV_{0.05}$ (SD 280 HV), respectively. The scattered hardness values of the carbides are attributed to the different grain sizes of the carbides radially inward.

The WC phase appears during the first 5 min of carburization, which is sooner than in the case of HWCVD of diamond (Zeiler et al., 2002). EDS corroborates the EBSD analysis on the presence of WC, disclosing that the layer is composed of 49.37 at% C and 50.63 at% W (SD 0.83). EBSD analysis reveals that the WC grains are randomly oriented, as shown in Figure 12. The size of the WC grains is

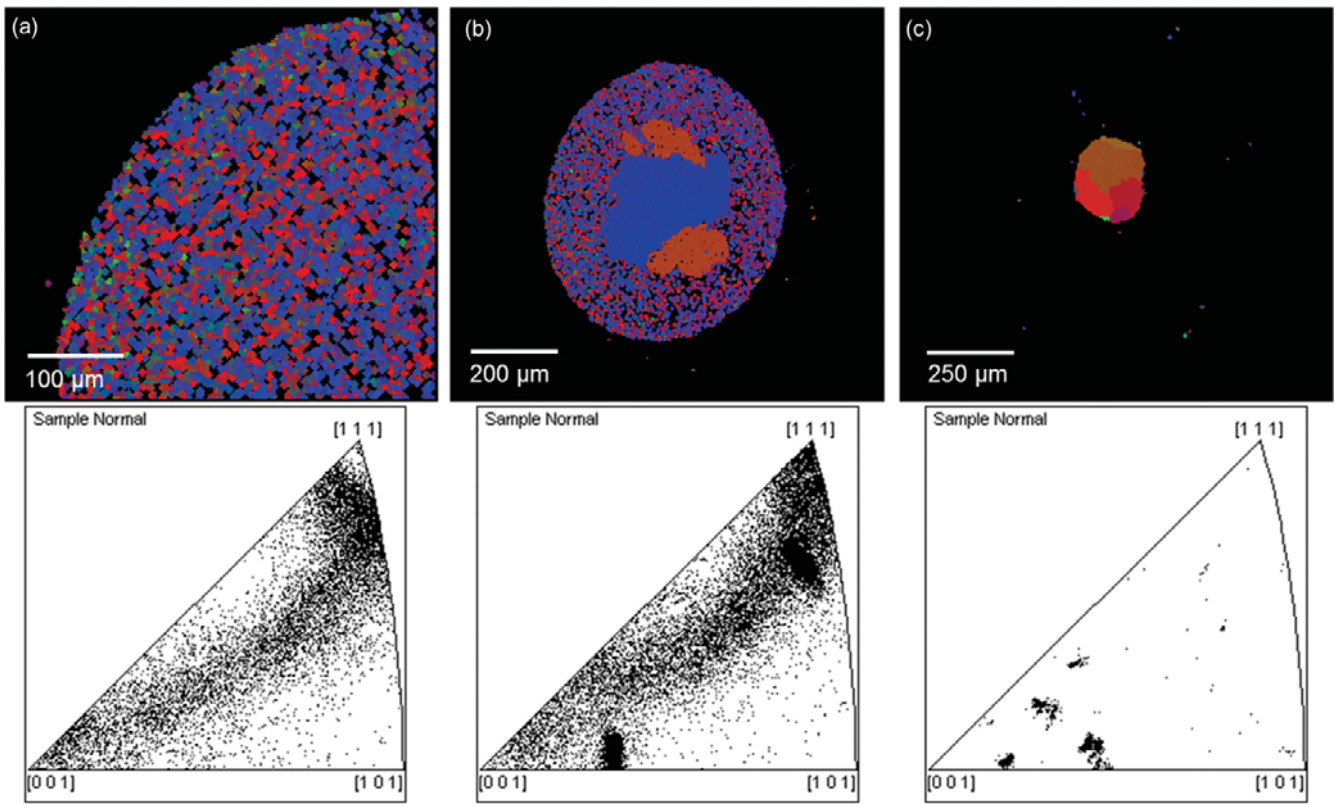

Figure 10. Grain orientation map of the W core at 30 min at (**a**) 1,400°C, (**b**) 1,600°C, and (**c**) 1,800°C. The inverse pole figures correspond to each orientation map directly above it.

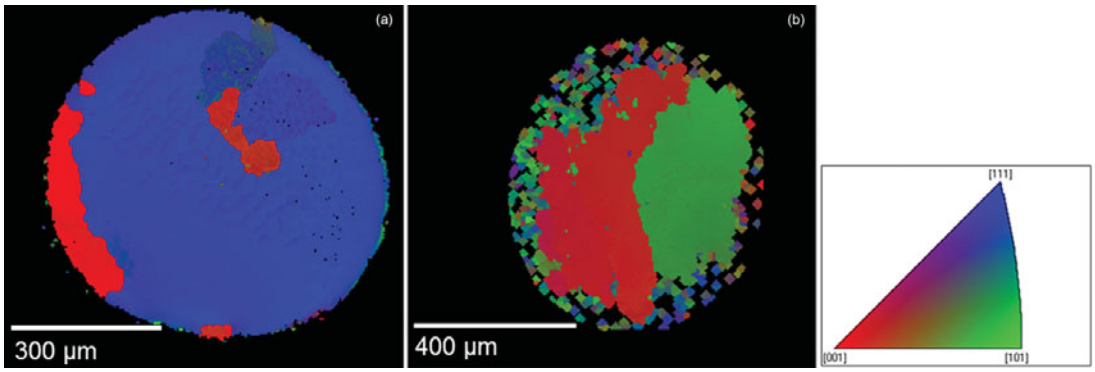

Figure 11. Grain orientation maps (with orientation key) of pure W-filaments after heated in (**a**) N_2 and in (**b**) H_2 ambient at a temperature of 2,000°C.

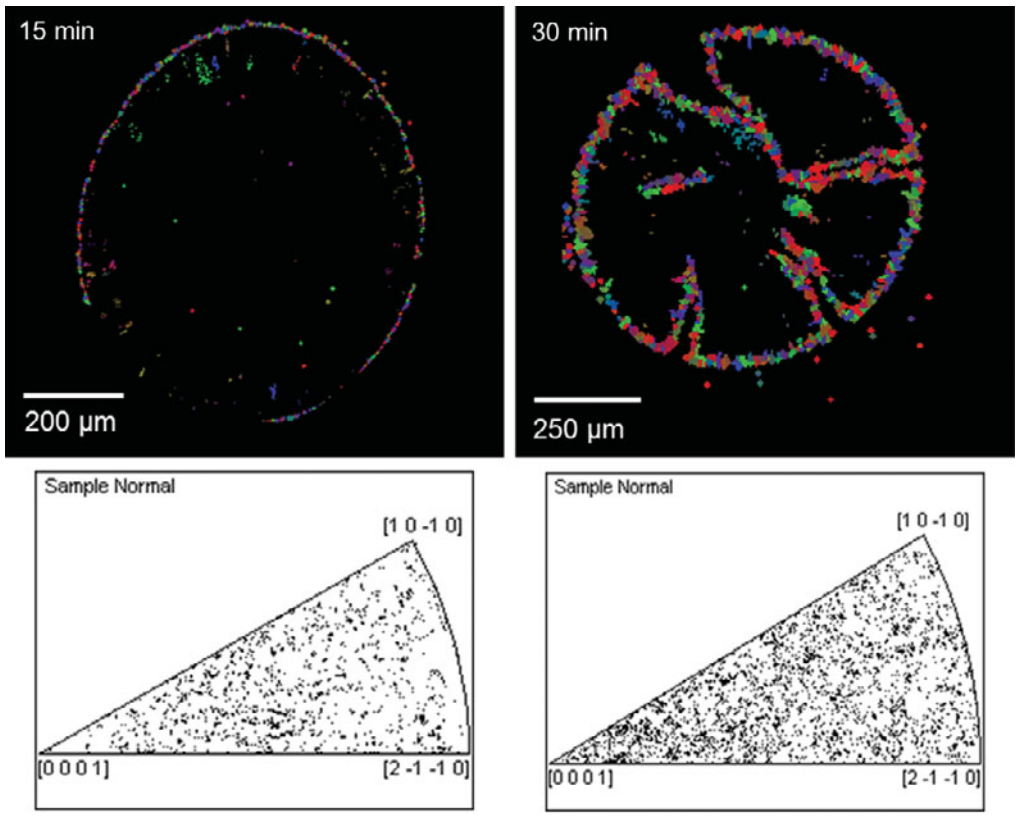

Figure 12. Grain orientation maps of the WC phase (with corresponding inverse pole figures below) at different times at T_{fil} = 2,000°C.

enhanced with prolonged carburization times and an increasing filament temperature.

Similar to the W_2C phase, the WC layer growth shows a parabolic rate constant. The activation energy of the WC growth amounted to 82.6 kJ/mol, as determined from an Arrhenius plot shown in Figure 13. Despite the superior growth rate of WC at $T_{fil} \leq 1{,}600$°C, the difference in the thicknesses of the WC and W_2C layers is minimal compared to $T_{fil} \geq 1{,}800$°C, as illustrated in Figure 14. Moreover, no crack formation occurred at 1,400°C, whereas cracks are prevalent throughout the W_2C layer at higher temperatures. These findings indicate that crack formation depends on the filament temperature.

Figure 15 shows secondary electron of the filament surface. Carbonaceous agglomerates appear on the filament surface during the formation of the WC phase, which eventually encapsulates the carburized filament. The appearance of these agglomerates is characteristic for the HWCVD of MWCNTs (Oliphant et al., 2009*b*) and is known as filament poisoning in the case of diamond deposition (Zeiler et al., 2002).

Figure 16 shows XRD patterns of the carburized W-filament. XRD corroborates the EBSD findings that the as-received W-filament is initially polycrystalline. At 5 min the W_2C and WC phases appear and their intensities enhance with prolonged carburization time. The graphitic

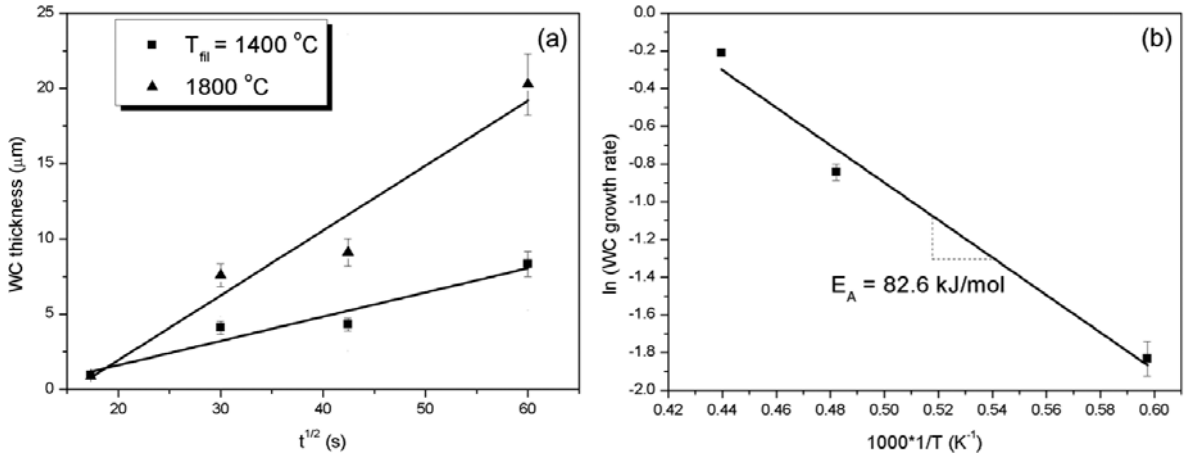

Figure 13. a: WC layer kinetics and (**b**) corresponding Arrhenius plot in the energy range between 1,400 and 2,000°C.

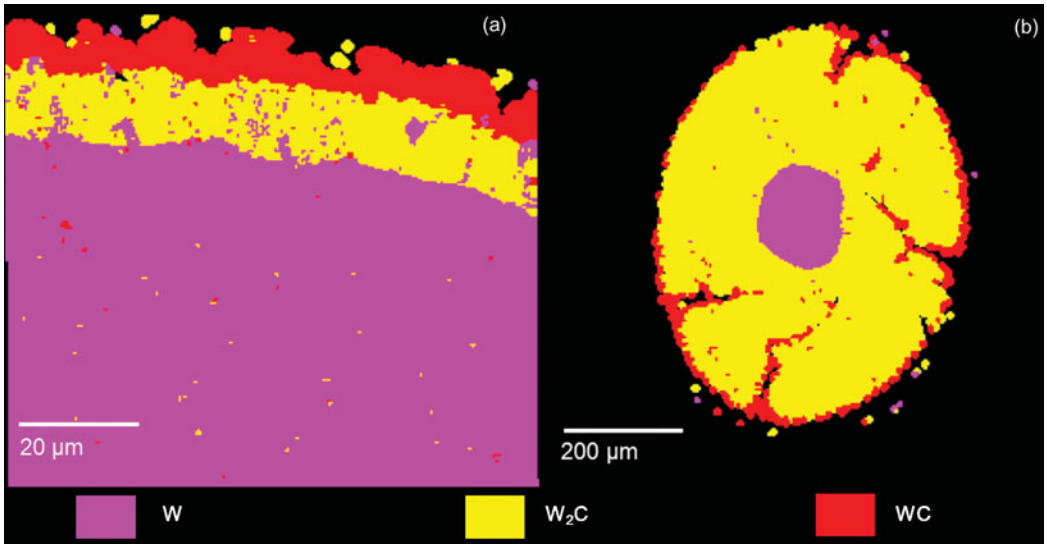

Figure 14. Electron backscatter diffraction phase maps of the filament carburized at (**a**) 1,400°C for 60 min and (**b**) at 1,800°C for 30 min.

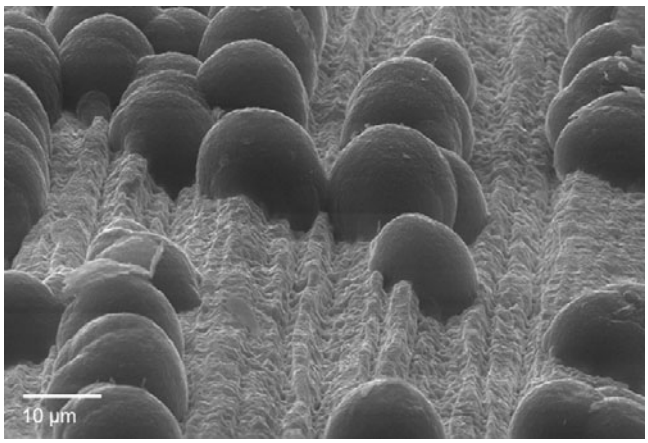

Figure 15. Secondary electron micrograph of the filament surface after exposure to the CH_4:H_2 ambient for 15 min at 2,000°C.

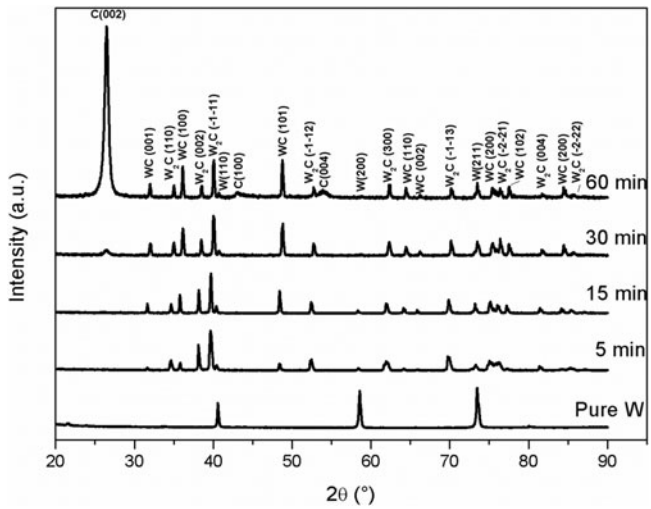

Figure 16. X-ray diffraction patterns of the W-filaments carburized for different durations at 2,000°C.

peak appears at 30 min and its intensity is enhanced significantly at 60 min. On the other hand, the intensities of the carbides remained relatively constant after 30 min once the graphite phase formed. The carbonaceous agglomerates observed on the filament surface are therefore graphitic.

Discussion

During the HWCVD of MWCNTs, the W filament surface reacts with C originating from the CH_4 gas. Subsequently, the C diffuses into the filament and eventually reaches concentrations suitable for the formation of W_2C. The growth of the W_2C phase follows a parabolic rate in the case of the HWCVD of MWCNTs, in contrast to diamond synthesis conditions where a linear relationship to time was found (Zeiler et al., 2002). The main differences in this study are the deposition pressure (approximately seven times higher) and CH_4 flow rate (ten times higher) (Zeiler et al., 2002). As a result, the supply of C at the filament-surface is greater resulting in a faster carburization process. The rate-determining step then becomes the diffusion of C through the carbide layer to the W_2C/W interface.

Generally, cracks appear during filament carburization owing to the expansion of the lattice by the incorporation of C, the subsequent volume expansion of the filament and the differences in density between W and its carbides that induces tension at the outer regions (Davidson et al., 1979; Zeiler et al., 2002). The microscopy results in this study reveal that cracks extend throughout the W_2C layer only when it reaches a thickness >30 μm and at $T_{fil} \geq 1{,}600$°C. The most likely reason is the presence of smaller grains at the filament perimeter at a W_2C thickness <30 μm, which reduces the formation and/or propagation of cracks from the surface radially inward. Additionally, at higher filament temperatures the difference in mechanical properties (e.g., thermal expansion) of the W phase and the carbides are enhanced and can also lead to crack formation.

The WC layer appears during the first 5 min. Similar to W_2C, the rate determining step is the diffusion of C; the difference is that the C must now diffuse through the WC layer to reach the WC/W_2C interface. The activation energy for the WC growth amounted to 82.6 kJ/mol, substantially lower than the reported value of 242 kJ/mol (McCarty et al., 1987). This discrepancy is because of the greater C concentration present at the conditions of the HWCVD of MWCNTs. Afterward, it becomes increasingly difficult for the C to diffuse through the thickening WC layer, eventually resulting in the deposition of graphite agglomerates on the filament surface. During the formation and growth of graphite on the filament surface, the C supply for carburization is reduced, resulting in saturating WC/W_2C XRD intensities. Additionally, the depletion of C from the ambient and eventual incorporation into the filament leads to an unstable supply rate of C necessary for the formation of MWCNTs.

Formation of the graphite phase on the filament surface during diamond deposition using HWCVD is known as filament poisoning as this leads to a reduction in the concentration of atomic hydrogen, which is considered to be crucial for the deposition of sp^3 hybridized C (Zeiler et al., 2002). The appearance of the graphite phase on the filament surface reduces the contact between the H_2 molecules and the catalytic W-carbide surface, leading to a reduction in the atomic hydrogen concentration. Consequently, this results in a reduction in the etching effect of atomic hydrogen, eventually leading to an enhancement of amorphous carbon deposits within MWCNT samples for $T_{fil} > 1{,}600$°C at a pressure of 20 kPa (Oliphant et al., 2009*b*). The importance of etching species such as atomic hydrogen and NH_2 for higher quality MWCNTs was also observed at lower deposition pressures of 0.1 kPa (Cojocaru et al., 2006).

A drop in temperature is noticed when the filament is exposed to an H_2 or CH_4:H_2 ambient. The temperature drop is attributed to a combination of the energy lost to dissociate H_2 into atomic hydrogen and CH_4 into C-containing reacting species (Langmuir, 1912; Zeiler et al., 2002), the formation of the graphite phase with its higher emissivity, the expanding filament diameter, and the presence of phases with different resistivities. As a result of the temperature drop, a thermal gradient can be established within the filament resulting in a hotter core. Consequently, the grain sizes of the W_2C and W phases are enhanced radially inward. Moreover, the recrystallizing W-core forms distinctive orientations in a H_2 and/or N_2 ambient as a result of different heat loss processes. The orientations and grain sizes of the recrystallizing W then determine its hardness.

The presence of the graphitic layer at $T_{fil} \geq 1{,}600$°C further reduces the heat-loss rate of the filament during the cooling down phase, bringing about larger differences in grain sizes and hardness values of the W_2C and W phases radially inward compared with lower filament temperatures. The stability of the filament during the HWCVD of MWCNTs depends on the extent of W-carbide formation (thickness and grain sizes) and the solid deposition of graphite on the filament surface, which are both enhanced at $T_{fil} \geq 1{,}600$°C. This confirms our earlier findings (Arendse et al., 2007; Oliphant et al., 2009*b*) that filament temperatures lower than ~2,000°C, which are typically used in the literature (Dillon et al., 2003), are more suitable for a stable HWCVD process of high-quality MWCNTs with minimal amorphous C deposits at our deposition conditions. In the case of exposing a heated W-filament to a C source, the extended filament operational lifetime and the minimal filament aging effect on the properties of the deposited material typically observed at lower deposition pressures (Tabata & Niato, 2011), may be achieved at higher deposition pressures by using filament temperatures below 1,600°C.

Conclusion

The carburization process of W filaments at the HWCVD conditions of MWCNTs were investigated using SEM, EDS, EBSD, AES, XPS, XRD, and microhardness measurements.

EBSD analysis, validated by XRD, showed conclusively that both the W_2C and WC phases formed during the first 5 min across the entire filament temperature range, with graphite agglomerates/layers forming on the filament surface at $T_{fil} \geq$ 1,600°C. The C and W elemental compositions disclosed by EDS, AES, and XPS analysis concur with each other on the presence of W, W_2C, and WC phases. Kinetic studies reveal that the diffusion of C through the growing carbide layer is the rate-determining step for the growth of the W_2C and WC layers. The activation energy for the formation of the WC layer amounted to 82.6 kJ/mol. The enhanced grain sizes of the W_2C and recrystallized W grains and corresponding differences in microhardness values were attributed to a thermal gradient resulting from the "cooling" of the filament in a H_2, CH_4:H_2 ambient, an encapsulating graphite layer, formation of phases with different resistivities, and an increasing filament diameter. Crack formation was influenced by the grain size, filament temperature, and the extent of the phases present with different properties. Filament temperatures <1,600°C promise to be more suitable for a stable MWCNTs deposition process at pressures of 20 kPa.

Acknowledgments

The authors acknowledge the financial support of the National Research Foundation (NRF) and the National Metrology Institute of South Africa.

References

Arendse, C.J., Malgas, G.F., Scriba, M.R., Cummings, F.R. & Knoesen, D. (2007). Effect of deposition pressure on the morphology and structural properties of carbon nanotubes synthesized by hot-filament chemical vapour deposition. *J Nanosci Nanotechnol* **7**, 3638–3642.

Chen, X., Hasegawa, M., Yang, S., Nitta, Y., Katsuno, T. & Motojima, S. (2008). Preparation of carbon microcoils by catalytic methane hot-wire CVD process. *Thin Solid Films* **516**, 714–717.

Cojocaru, C.S., Kim, D., Pribat, D. & Bourée, J.E. (2006). Synthesis of multi-walled carbon nanotubes by combining hot-wire and dc plasma-enhanced chemical vapour deposition. *Thin Solid Films* **501**, 227–232.

Davidson, C.F., Alexander, G.B. & Wadsworth, M.E. (1979). Catalytic effect of cobalt on the carburization kinetics of tungsten. *Metall Trans A* **10**, 1059–1069.

Dillon, A.C., Mahan, A.H., Parilla, P.A., Alleman, J.L., Heben, M.J., Jones, K.M. & Gilbert, K.E.H. (2003). Continuous hot wire chemical vapour deposition of high-density carbon multiwall nanotubes. *Nano Lett* **3**, 1425–1429.

Kawale, S.S., Bhardwaj, S., Kshirsagar, D.E., Bhosale, C.H., Sharon, M. & Sharon, M. (2011). Thin films of carbon nanomaterial from natural precursor by hot-wire CVD. *Fullerenes, Nanotubes, Carbon Nanostruct* **19**, 540–549.

Knoesen, D., Arendse, C., Halindintwali, S. & Muller, T. (2008). Extension of the lifetime of tantalum filaments in the hot-wire (Cat) chemical vapour deposition process. *Thin Solid Films* **516**, 822–825.

Kromka, A., Janík, J., Šatka, A., Pavlov, J. & Červeň, I. (2001). Investigation of carburization of tungsten-carbide formation by hot-filament CVD technique. *Acta Phys Slovaca* **51**, 359–368.

Kurlov, A.S. & Gusev, A.I. (2006). Phase equilibria in the W-C system and tungsten carbides. *Russ Chem Rev* **75**, 617–636.

Langmuir, I. (1912). The dissociation of hydrogen into atoms. *J Am Chem Soc* **34**, 860–877.

Lassner, E. & Schubert, W. (1999). *Tungsten: Properties, Chemistry, Technology of the Element, Alloys, and Chemical Compounds*, pp. 18 and 20. New York: Kluwer Academic/Plenum Publishers.

Mahan, A.H., Carapella, J., Nelson, B.P., Crandall, R.S. & Balberg, I. (1991). Deposition of device quality, low H content amorphous silicon. *J Appl Phys* **69**, 6728–6730.

McCarty, L.V., Donelson, R. & Hehemann, R.F. (1987). A diffusion model for tungsten powder carburization. *Metall Trans A* **18**, 969–974.

Moustakas, T.D. (1989). The role of the tungsten filament in the growth of polycrystalline diamond films by filament-assisted CVD of hydrocarbons. *Solid State Ionics* **32–33**, 861–868.

Oliphant, C.J., Arendse, C.J., Malgas, G.F., Motaung, D.E., Muller, T.F.G., Halindintwali, S., Julies, B.A. & Knoesen, D. (2009*a*). Filament poisoning at typical carbon nanotube deposition conditions by hot-filament CVD. *J Mater Sci* **44**, 2610–2616.

Oliphant, C.J., Arendse, C.J., Malgas, G.F., Motaung, D.E., Muller, T.F.G. & Knoesen, D. (2009*b*). Dual catalytic purpose of the tungsten filament during the synthesis of single helix carbon microcoils by hot-wire CVD. *J Nanosci Nanotechnol* **9**, 5870–5873.

Oliphant, C.J., Arendse, C.J., Prins, S.N., Malgas, G.F. & Knoesen, D. (2012). Structural evolution of a Ta-filament during hot-wire chemical vapour deposition of silicon investigated by electron backscatter diffraction. *J Mater Sci* **47**, 2405–2410.

Pryce Lewis, H.G., Bansal, N.P., White, A.J. & Handy, E.S. (2009). HWCVD of polymers: Commercialization and scale-up. *Thin Solid Films* **517**, 3551–3554.

Shi, Y.L., Tong, L., Eustergerling, B.D. & Li, X.M. (2011). Silicidation and carburization of the tungsten filament in HWCVD with silacyclobutane precursor gases. *Thin Solid Films* **519**, 4442–4446.

Tabata, A. & Niato, A. (2011). Structural changes in tungsten wire and their effect on the properties of hydrogen nanocrystalline cubic silicon carbide thin films. *Thin Solid Films* **519**, 4451–4454.

van der Werf, C.H.M., Li, H., Verlaan, V., Oliphant, C.J., Bakker, R., Houweling, Z.S. & Schropp, R.E.I. (2009). Reversibility of silicidation of Ta filaments in HWCVD of thin film silicon. *Thin Solid Films* **517**, 3431–3434.

Zeiler, E., Schwarz, S., Rosiwal, S.M. & Singer, R.F. (2002). Structural changes of tungsten heating filaments during CVD of diamond. *Mater Sci Eng A* **335**, 236–245.